Journal of Materials Chemistry A

COMMUNICATION

View Article Online
View Journal | View Issue

Cite this: J. Mater. Chem. A, 2015, 3, 488

Received 29th October 2014
Accepted 21st November 2014

DOI: 10.1039/c4ta05769d

www.rsc.org/MaterialsA

Interconnected three-dimensional V_2O_5/polypyrrole network nanostructures for high performance solid-state supercapacitors†

Tao Qian,‡ Na Xu,‡ Jinqiu Zhou, Tingzhou Yang, Xuejun Liu, Xiaowei Shen, Jiaqi Liang and Chenglin Yan*

Supercapacitor electrodes composed of a 3D V_2O_5 network with polypyrrole (PPy) uniformly decorated onto each nanowire were fabricated to enhance their pseudocapacitive performance. The continuous 3D network creates channels for better ion transport, and the high degree of pore connectivity in the network enhances the mass transport. The PPy shell could enhance the electric conductivity and prevent the dissolution of vanadium. These merits together with the ideal synergy between V_2O_5 and PPy lead to a high specific capacitance of 448 F g^{-1}, which is three times higher than that of the stacked V_2O_5. The all-solid-state symmetric supercapacitor device assembled by the V_2O_5/PPy core/shell 3D network exhibits a high energy density (14.2 W h kg^{-1}) at a power density of 250 W kg^{-1} and good cyclic stability (capacitance retention of 81% after 1000 cycles). Furthermore, the prepared device could power a red light-emitting diode indicator efficiently after charging for only 10 s.

Introduction

Supercapacitors, also called electrochemical capacitors or ultracapacitors, are a class of electrochemical energy storage devices exhibiting high power density, long cycling life, and excellent reversibility.[1–4] Supercapacitors can be classified into two types based on their charge-storage mechanism: double layer capacitors with carbon electrodes and pseudocapacitors with metal oxide or conducting polymer electrodes.[5,6] For pseudocapacitors, properties such as high specific surface area, high electrical conductivity and fast diffusion properties are important to achieve high power density and energy density. Transition-metal oxides such as RuO_2,[7] MnO_2,[8] Co_3O_4,[9] NiO,[10] and V_2O_5 (ref. 11 and 12) have higher capacity than electrochemical double-layer capacitive carbon materials due to their unique redox reaction. Among various transition-metal oxides, V_2O_5 possesses the advantages of high energy density,[13] natural abundance, low cost, unique layered structures and wide potential windows arising from its various vanadium oxidation states (V^{2+}, V^{3+}, V^{4+}, and V^{5+}).[14] Many efforts have been made to fabricate different nanostructures of V_2O_5 such as nanoribbons,[15] nanotubes,[16] nanorods,[17] nanosheets,[18] and nanowires,[19] which have been demonstrated to be effective to improve the performance of V_2O_5-based supercapacitors. However, the problems of the poor structural stability (due to the V_2O_5 dissolution in the aqueous electrolyte), low conductivity and slow electrochemical kinetics of V_2O_5 which limit the specific capacity and long-term cycling stability have not been solved well.[20,21]

On the other hand, combining V_2O_5 with carbon materials has been justified to be an effective method to improve the electric transport properties of V_2O_5,[6,22] but the cyclic stability is still undesirable because such combinations cannot prevent the dissolution of vanadium which leads to the loss of active materials. Polypyrrole (PPy) is an intrinsically conductive polymer as a pseudocapacitor material because of its high conductivity, storage ability, redox and capacitive current and good thermal and environmental stability.[23–25] To solve the above issues, in the current work, we have developed interconnected 3D V_2O_5 network nanostructures constructed through a "seeding approach" by a Ni substrate, which can afford to drastically optimize the morphology of the as-produced V_2O_5. The prepared V_2O_5 then promoted the *in situ* polymerization process by oxidizing the pyrrole monomer into 3D network forms, and V_2O_5/PPy interconnected core–shell structures were obtained. The continuous 3D network creates channels for better ion transport to the redox-active material, and the high degree of pore connectivity in the network enhances the mass transport as well as increases the material lifetime of the device. The decorated PPy shell simultaneously utilizes the high electronic conductivity of PPy with respect to that of V_2O_5 and the

College of Physics, Optoelectronics and Energy & Collaborative Innovation Center of Suzhou Nano Science and Technology, Soochow University, Suzhou 215006, China. E-mail: c.yan@suda.edu.cn

† Electronic supplementary information (ESI) available. See DOI: 10.1039/c4ta05769d

‡ The first two authors contributed equally to this work.

polymeric coating effect of PPy to prevent the dissolution of vanadium. As a result, the 3D V_2O_5/PPy core/shell network exhibits a remarkably enhanced specific capacitance of 448 F g^{-1}, which is over three times higher than that of the stacked V_2O_5 nanostructures. The improved capacitance retention of 81% was maintained after 1000 cycles, which is better than those of the reported V_2O_5 nanowires, nanotubes, and nanoflowers.

Experimental section

Synthesis of V_2O_5 network nanostructures

60 mL sodium metavanadate solution (1 M) was dropped onto a Ni substrate through an ion-exchange column, and then allowed to stand overnight. The products were collected by centrifugation and crystallization at 400 °C for 2 h.

Synthesis of V_2O_5/PPy core/shell network nanostructures

10 μL hydrogen peroxide (30 wt%) was added to a mixture of 50 mg as-prepared V_2O_5 network, 5 μL pyrrole, and 10 mL deionized water. The PPy shell could decorate on the porous V_2O_5 network uniformly after 12 h of vigorous stirring.

Structure characterization

The morphology of the nanostructures was investigated by field emission scanning electron microscopy (FESEM, SU8010, Japan) and field emission transmission electron microscopy (FETEM, FEI Tecnai G220, America). Surface elemental analysis was performed on an X-ray photoelectron spectrometer (XPS, Kratos Axis Ultra Dld, Japan).

Electrochemical characterization

Electrochemical tests were carried out using a CHI 660E (Chenhua Shanghai, China) electrochemical workstation. The working electrodes were prepared by making a slurry of 70 wt% active materials, 20 wt% acetylene black, and 10 wt% polytetrafluoroethylene (PTFE, 60 wt% dispersion in water) in ethanol. The obtained slurry was then coated onto titanium foil as a current collector within an area of 1 × 3 cm^2 and areal mass of 0.25 mg cm^{-2}, which were then dried in a vacuum at 60 °C for 12 h to remove the solvent. Cyclic voltammetry (CV), charge–discharge and electrochemical impedance spectroscopy (EIS) were performed in three-electrode and two-electrode systems, respectively. In half-cell tests, a three-electrode system was used to measure the response of the V_2O_5/PPy network, where the prepared electrode served as a working electrode using 5 M $LiNO_3$ aqueous solution as the electrolyte, with a Pt mesh as the counter electrode and Ag/AgCl as the reference electrode. In full cell tests, the supercapacitor was assembled to measure the device performance. In detail, the $LiNO_3$/PVA (polyvinyl alcohol) gel electrolyte was prepared as follows: 6.9 g of $LiNO_3$ and 3 g of PVA were added into 20 mL of deionized water, and then the whole mixture was heated to 90 °C under stirring until the solution became clear. To assemble a solid-state symmetric supercapacitor, two pieces of the prepared electrodes were assembled with an ~120 μm thick membrane (DR2012, Suzhou Beige New Materials & Technology Co. Ltd.) saturated with $LiNO_3$/PVA gel as the separator, sandwiched in between (Fig. 4A). The total thickness of the devices was less than 0.4 mm.

Results and discussion

The fabrication technique essentially consists of two parts (Fig. S1†). Firstly, the V_2O_5 network was synthesized through a "seeding approach" with a Ni substrate, the reaction process can be expressed as:

$$Ni + 2HVO_3 \rightarrow Ni(VO_3)_2 + H_2\uparrow \quad (1)$$

$$Ni(VO_3)_2 + H_2O \rightarrow Ni(OH)_2 + V_2O_5 \quad (2)$$

$$2HVO_3 \rightarrow V_2O_5 + H_2O \quad (3)$$

where steps (1, 2) illustrate that the "seeds" are obtained by double hydrolysis of $Ni(VO_3)_2$; step (3) reveals the growth process of V_2O_5 which occupied the main component of the network. Secondly, the pyrrole monomer was polymerized into the 3D network formed by oxidation.

To investigate the morphology of the fabricated 3D V_2O_5/PPy core/shell network, scanning electron microscopy (SEM) and transmission electron microscopy (TEM) images were obtained and results are shown in Fig. 1. It is apparent that the 3D V_2O_5 network can be constructed through a "seeding approach" (Fig. 1A). The magnified SEM image (Fig. 1B) further reveals the detailed morphology of the V_2O_5 network which is composed of nanowires. The SEM image of the V_2O_5/PPy core/shell network

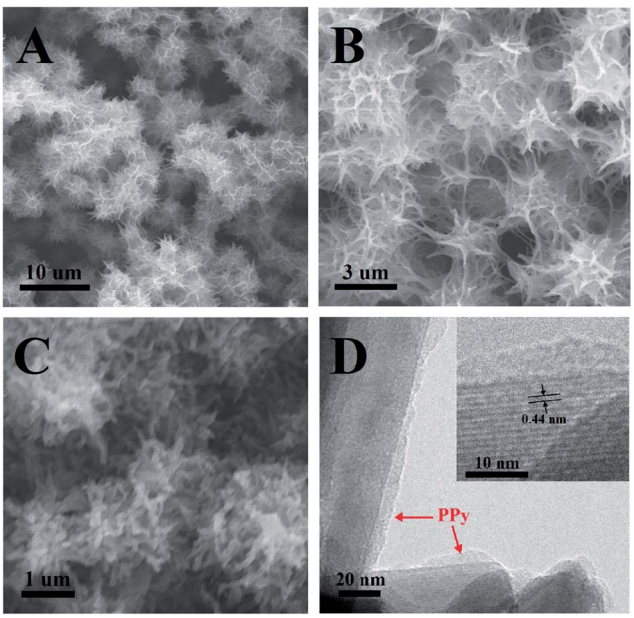

Fig. 1 (A) Low-magnification and (B) high-magnification SEM images of the V_2O_5 network. (C) High-magnification SEM images of the V_2O_5/PPy core/shell network and (D) the HRTEM image of the surface of V_2O_5/PPy core/shell network. The inset shows the V_2O_5 crystal lattice and amorphous PPy structures.

shown in Fig. 1C illustrates that the integration of PPy into the network does not deteriorate the ordered structure. TEM images (Fig. 1D) of the V_2O_5/PPy network further prove that core/shell structures with the PPy film uniformly formed on the V_2O_5 nanowire surface are obtained. The inset shows the amorphous PPy shell structures and inner V_2O_5 crystalline structures with a lattice spacing of 0.44 nm in detail.

X-ray photoelectron spectroscopy (XPS) spectra of the V_2O_5 and V_2O_5/PPy network were investigated as shown in Fig. 2A. In the survey region from 200 to 900 eV, it is evident that V, O, and Ni elements all exist in the sample of the V_2O_5 network before PPy coating. From careful inspection of wide region spectroscopy and elemental analysis, it could be observed that for the V_2O_5/PPy hybrid network, the peak of N1s appears at 399.57 eV (also shown in Fig. 2B) and the peak intensity of C1s at 284.42 eV is enhanced, which both indicate the existence of PPy. Fig. 2C and D reveal the high-resolution spectra of V and Ni for the V_2O_5/PPy hybrid network. The two peaks were assigned to $V2p_{3/2}$ and $V2p_{1/2}$ at the binding energy of 516.72 eV and 524.57 eV, respectively (Fig. 2C), implying the formation of the V_2O_5 phase in the nanocomposite matrix.[5,15] From Fig. 2D, the only one peak at 855.32 eV corresponding to Ni2p was observed, which justifies the presence of $Ni(OH)_2$.[26] These results demonstrate that the V_2O_5 network was successfully fabricated by seeding of a Ni substrate and coating it with a PPy shell.

To explore the potential application of the electrode material for supercapacitors, CV curves of the stacked V_2O_5, V_2O_5 network, and V_2O_5/PPy core/shell network at different scan rates are shown in Fig. S2A–C,† respectively. All of the figures show well-resolved two pairs of cathodic and anodic peaks which are very distinct from those of the electric double-layer capacitance in which the curve shape is normally close to an ideal rectangular shape, and the current of the electrode responds quasi-linearly with increasing potential scan rate, demonstrating its excellent reactivity.[27] Comparison among three different electrode materials is demonstrated by CV curves at a scan rate of 100 mV s^{-1} in Fig. S2D.† For the V_2O_5 network, cathodic and anodic peaks could be distinguished much more obviously in contrast to that of the stacked V_2O_5, such a network structure with ultrafine wires and multilevel pores is favorable for providing easy access of the electrolyte to the materials and large electroactive surface that is advantageous in energy storage applications.[28] However, the CV curve of the V_2O_5/PPy core/shell network expands distinctly with larger integral area in comparison with that of the V_2O_5 network, certifying the preferable capacitor performance attributable to the improved electronic conductivity of the nanocomposite derived from PPy coating. The above phenomena demonstrate that the V_2O_5 network coated with a PPy shell exhibits remarkable electrochemical performance for supercapacitor electrodes.

Galvanostatic charge/discharge experiments at different current densities were performed to estimate the specific capacitance of the stacked V_2O_5, V_2O_5 network, and V_2O_5/PPy core/shell network as supercapacitor electrodes (Fig. 3A–C). Two well-defined plateaus during the discharge processes are observed in all of the figures revealing their satisfactory pseudocapacitive behavior. The electrochemical Li^+ insertion process occurring at V_2O_5 electrodes can be expressed as:

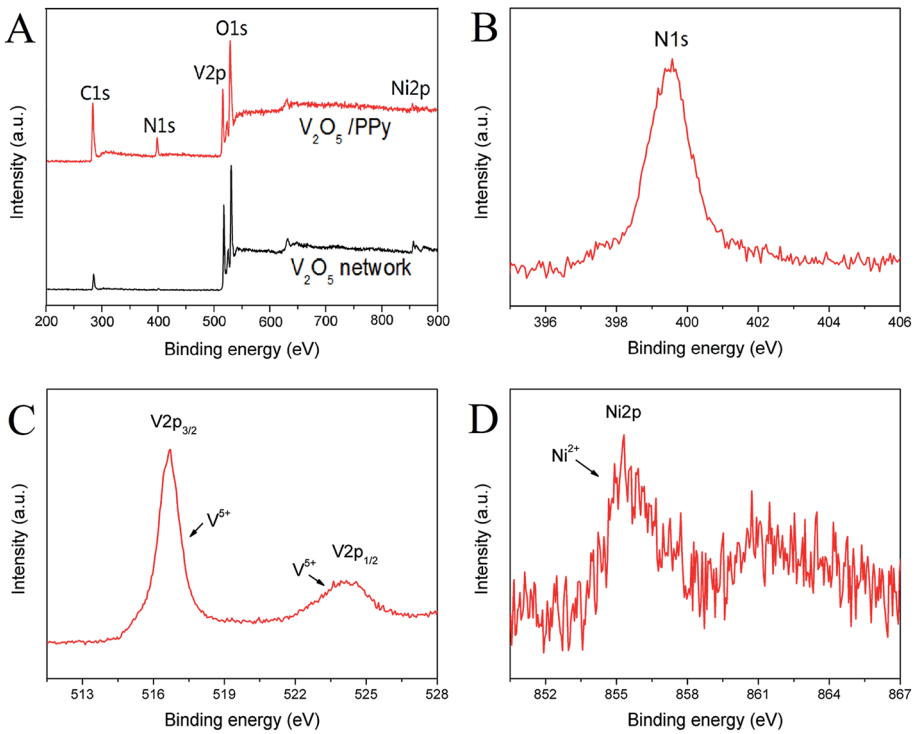

Fig. 2 (A) Full X-ray photoelectron spectroscopy (XPS) spectra of the V_2O_5 and V_2O_5/PPy core/shell networks. The high resolution (B) N1s, (C) V2p and (D) Ni2p XPS spectra.

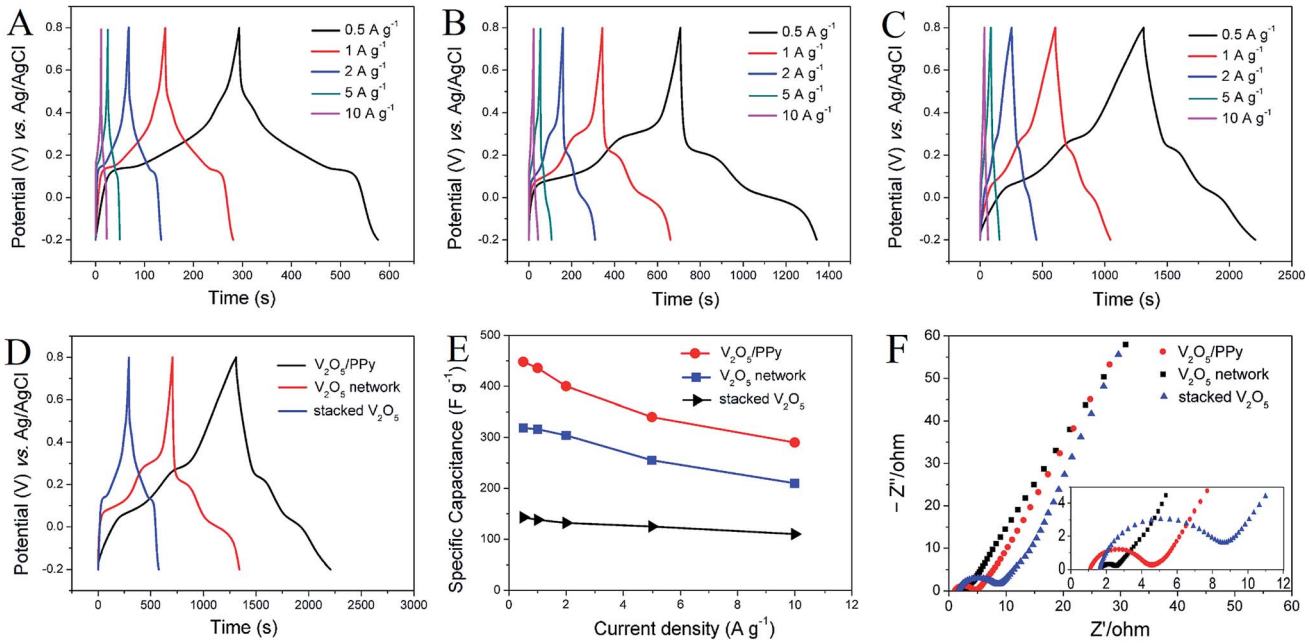

Fig. 3 Galvanostatic charge/discharge curves of the prepared (A) stacked V_2O_5, (B) V_2O_5 network, and (C) V_2O_5/PPy core/shell network electrode at current densities of 0.5, 1, 2, 5, 10 A g^{-1}. (D) Galvanostatic charge/discharge curves of three different materials at a scan rate of 0.5 A g^{-1}. (E) Specific capacitances of three different materials at different current densities. (F) Nyquist plots of the three prepared different material electrodes.

$$V_2O_5 + xLi^+ + xe^{-1} \leftrightarrow Li_xV_2O_5 \quad (4)$$

where x is the mole fraction of inserted Li^+ ions. The typical galvanostatic charge/discharge curves of the stacked V_2O_5, V_2O_5 network, and V_2O_5/PPy core/shell network measured at a current density of 0.5 A g^{-1} are shown in Fig. 3D for comparison. The two discharge plateaus of the V_2O_5/PPy core/shell network are much distinguished and the discharge time is much larger than that of the stacked V_2O_5 and V_2O_5 network, demonstrating higher electrochemical activity behavior. Furthermore, the specific capacitance (C_m) of the device is calculated by the following equation:

$$C_m = I\Delta t/m\Delta E \quad (5)$$

where I is the discharge current, Δt is the discharge time, ΔE is the potential window during the discharge process, and m is the effective electrode mass.[29] In the case of the V_2O_5/PPy core/shell network, a high specific capacitance of 448 F g^{-1} is obtained at a current density of 0.5 A g^{-1} which is much higher than those of the V_2O_5 network (318.5 F g^{-1}) and stacked V_2O_5 (143 F g^{-1}) under the same testing conditions (Fig. 3E). These results demonstrate that the 3D network structure with the PPy shell is preferable to improve the capacitive performance of V_2O_5 base-materials.

EIS measurement in the frequency range of 10 mHz to 1000 kHz was performed to clearly understand the ion diffusion of the electrodes (Fig. 3F). The Nyquist plots of the electrodes all show the form with a semicircle in the higher frequency region and spike in the lower frequency region which is characteristic of the capacitive behavior. The ohmic resistance of the electrolyte and the electrode materials is denoted as R_S, which is the intersection of the curve at the real part. The interfacial charge transfer resistance (R_{CT}) is connected to represent the semicircle in the high frequency region.[30] For the V_2O_5 network electrode, it shows the same R_S (~1.65 Ω) and the smaller R_{CT} (~0.8 Ω) compared with those of stacked V_2O_5 (R_{CT} ~ 7 Ω) because the network structure is beneficial to accelerate the charge transfer. In the case of the V_2O_5/PPy core/shell network, R_S is only ~1.09 Ω, which is much lower than that of V_2O_5 network (~1.65 Ω) electrodes, clearly demonstrating the high conductivity after PPy coating. However, the R_{CT} (~3.5 Ω) is larger than that of the V_2O_5 network, which is attributed to the inhibition of the charge transfer of the PPy coating.

To further explore the advantages of the prepared materials for real applications, the symmetric supercapacitor was assembled from two pieces of 3D V_2O_5/PPy core/shell network, each with a mass loading of 0.75 mg, as shown in Fig. 4A. Fig. 4B shows the CV curves in the potential window between 0 and 1 V, which present essentially the same nearly rectangular shape as the scan rate increases from 5 to 100 mV s^{-1}, indicating the good capacitive behavior of the device. Furthermore, the charge/discharge curves are similar in shape between 0 and 1 V at different current densities from 0.5 to 10 A g^{-1} (Fig. 4C), illustrating that the supercapacitor can be stably performed in a wide range of current densities. Nyquist plots of the symmetric supercapacitor were obtained (as shown in Fig. S3†), which reveal the same R_S (~1.09 Ω) and higher R_{CT} (~8.5 Ω), as compared with those of the prepared electrode in aqueous electrolytes. The main reason is due to the fact that the gel electrolyte and diaphragm do not take advantage of the charge transfer between the electrodes.

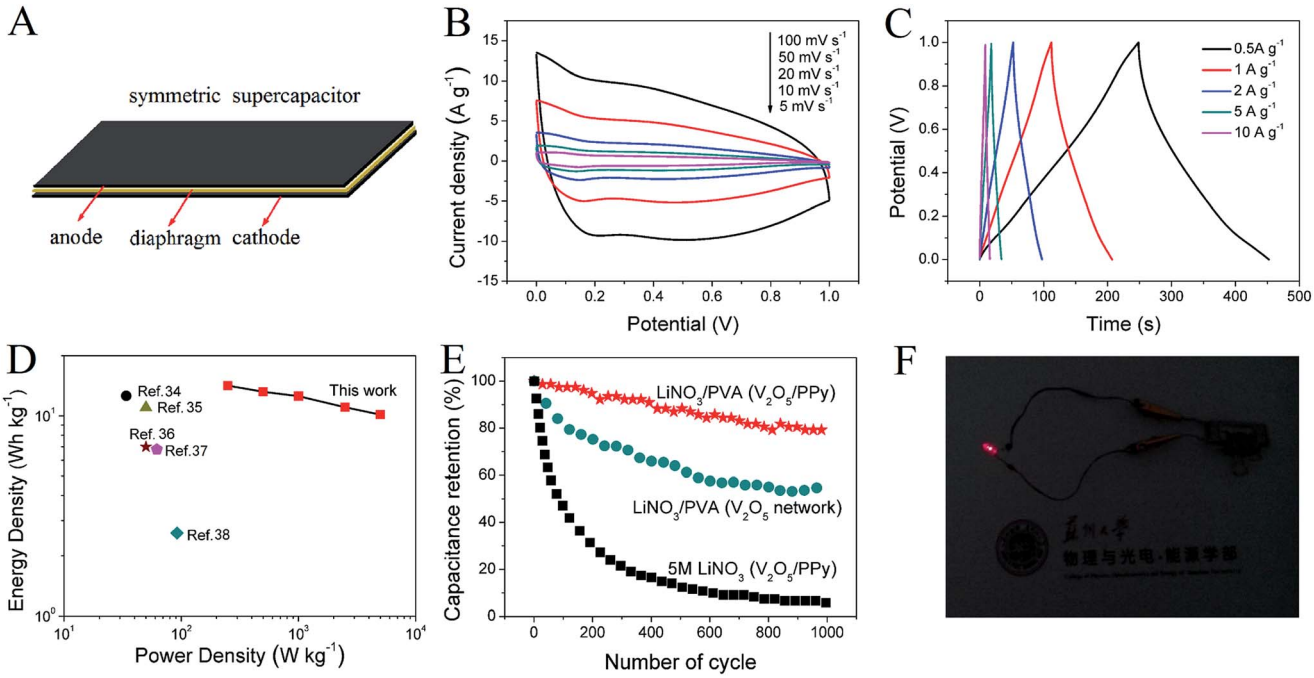

Fig. 4 (A) Schematic illustration of the symmetric supercapacitor configuration. (B) CVs and (C) charge–discharge curves of the symmetric supercapacitor. (D) Ragone plots of the solid-state V_2O_5/PPy devices. The values reported for other devices are added for comparison.[34–38] (E) Cycling performance of a single V_2O_5/PPy electrode and symmetric V_2O_5/PPy device collected at a current density of 10 A g^{-1} for 1000 cycles in 5 M $LiNO_3$ aqueous solution and the $LiNO_3$/PVA gel electrolyte, respectively. (F) A picture showing that the supercapacitor can lighten up a LED indicator.

Ragone plots of the device describing the relationship between energy density and power density were obtained, which is shown in Fig. 4D. The power densities and energy densities of the symmetric supercapacitor used in this work were collected to compare with the values reported for other metal oxide-based supercapacitor devices. The Ragone plots show that the energy density and power density of the prepared device are considerably higher than those of metal oxide-based supercapacitor devices. Moreover, the supercapacitor also shows excellent rate behavior, with an energy density of 10.14 W h kg^{-1} at a power density of 5000 W kg^{-1}.

We fabricated symmetric supercapacitors based on the as-prepared V_2O_5/PPy core/shell network and investigated their cycling stability in both 5 M $LiNO_3$ aqueous solution and $LiNO_3$/PVA gel electrolyte. Fig. 4E illustrates the specific capacitance retention as a function of cycle number, the capacitance of the V_2O_5/PPy core/shell network electrode decreases continuously in aqueous solution, and only about 5.7% of the initial capacitance is retained after 1000 cycles. The poor cycling performance of electrodes is mainly due to the instability of V_2O_5 in aqueous electrolytes and the ease of the formation of highly soluble complexes.[31,32] The PPy shell could prevent it from dissolution in the aqueous electrolyte, but cannot completely solve the dissolution problem. Therefore, the cycling stability is still not desirable due to the interaction between V_2O_5 and the aqueous electrolyte. To address this issue, replacing the aqueous electrolyte with a gel electrolyte with very low moisture content can be one of the solutions to improve the stability. Significantly, the $LiNO_3$/PVA gel electrolyte prominently improves the stability of the device, with a capacitance retention of 81.2% after 1000 cycles, because the gel electrolyte could prevent the chemical dissolution of vanadium oxides by minimizing the water content, and avoid the structure pulverization of vanadium oxides by holding the direct contact between electrochemically active materials and substrates during cycling.[33] Furthermore, the cyclic stability of the as-prepared device stands in sharp contrast to 48.8% of capacitance loss for the supercapacitor based on the V_2O_5 network. The improved stability is due to the fact that the PPy shell coated on the V_2O_5 nanowires prevents vanadium dissolution into the electrolyte. To further assess the application value of the 3D V_2O_5/PPy core/shell network, we assembled supercapacitors, and charged it for only 10 s to ~2 V, the devices could power red light-emitting diode (LED) (5 mm diameter 1.8 V, 20 mA) indicators efficiently (Fig. 4F).

Conclusions

The fabrication of the 3D V_2O_5/PPy interconnected core/shell network nanostructures has been developed with an excellent capacitive performance of 448 F g^{-1} arising from the synergetic effect from the V_2O_5 network and conductive PPy shell. The continuous 3D V_2O_5/PPy network creates channels for better ion transport, and the PPy shell could effectively enhance the electronic conductivity and prevent the dissolution of vanadium. Two-electrode symmetric supercapacitors based on V_2O_5/PPy

core/shell network electrodes further deliver high specific energy and power densities, as well as exhibit outstanding cycling life. Furthermore, the simple and cost-effective assembly of the supercapacitor electrodes illustrates potential applications in small warning light, clock chips, and wearable electronic devices.

Acknowledgements

We acknowledge the support from the "Thousand Talents Program", the Natural Science Foundation of Jiangsu Province of China (no. BK20140315), the National Natural Science Foundation of China (no. 51402202), the National Basic Research Program of China (no. 2015CB358600), Jiangsu shuangchuang plan, and the Priority Academic Program Development of Jiangsu Higher Education Institutions (PAPD).

Notes and references

1 S. D. Perera, A. D. Liyanage, N. Nijem, J. P. Ferrarus, Y. J. Chabal and K. J. Balkus, *J. Power Sources*, 2013, **230**, 130.
2 D. Choi, G. E. Blomgren and P. N. Kumta, *Adv. Mater.*, 2006, **18**, 1178.
3 Y. W. Zhu, S. Murali, M. D. Stoller, K. J. Ganesh, W. W. Cai, P. J. Ferreira, A. Pirkle, R. M. Wallace, K. A. Cychosz, M. Thommes, D. Su, E. A. Stach and R. S. Ruoff, *Science*, 2011, **332**, 1537.
4 M. L. Li, G. Y. Sun, P. P. Yin, C. P. Ruan and K. Ai, *ACS Appl. Mater. Interfaces*, 2013, **5**, 11462.
5 G. P. Wang, L. Zhang and J. J. Zhang, *Chem. Soc. Rev.*, 2012, **41**, 797.
6 C. Y. Foo, A. Sumboja, D. J. H. Tan, J. H. Wang and P. S. Lee, *Adv. Energy Mater.*, 2014, **10**, 1002.
7 C. C. Hu, W. C. Chen and K. H. Chang, *J. Electrochem. Soc.*, 2004, **151**, A281.
8 J. Yan, E. Khoo, A. Sumboja and P. S. Lee, *ACS Nano*, 2010, **4**, 4247.
9 Z. S. Wu, W. C. Ren, L. Wen, L. B. Gao, J. P. Zhao, Z. P. Chen, G. M. Zhou, F. Li and H. M. Cheng, *ACS Nano*, 2010, **4**, 3187.
10 J. W. Lang, L. B. Kong, W. J. Wu, Y. C. Luo and L. Kang, *Chem. Commun.*, 2008, **35**, 4213.
11 A. M. Glushenkov, D. Hulicova-Jurcakova, D. Llewellyn, G. Q. Lu and Y. Chen, *Chem. Mater.*, 2010, **22**, 914.
12 X. H. Lu, M. H. Yu, T. Zhai, G. M. Wang, S. L. Xie, T. Y. Liu, C. L. Liang, Y. X. Tong and Y. Li, *Nano Lett.*, 2013, **13**, 2628.
13 G. D. Nie, X. F. Lu, J. Y. Lei, Z. Q. Jiang and C. Wang, *J. Mater. Chem. A*, 2014, **2**, 15495.
14 S. Boukhalfa, K. Evanoff and G. Yushin, *Energy Environ. Sci.*, 2012, **5**, 6872.
15 Q. T. Qu, Y. S. Zhu, X. W. Gao and Y. P. Wu, *Adv. Energy Mater.*, 2012, **2**, 950.
16 Y. S. Hu, X. Liu, J. O. Muller, R. Schlogl, J. Maier and D. S. Su, *Angew. Chem., Int. Ed.*, 2009, **48**, 210.
17 A. Q. Pan, J. G. Zhang, Z. M. Nie, G. Z. Cao, B. W. Arey, G. S. Li, S. Q. Liang and J. Liu, *J. Mater. Chem.*, 2010, **20**, 9193.
18 A. Q. Pan, H. B. Wu, L. Zhang and X. W. Lou, *Energy Environ. Sci.*, 2013, **6**, 1476.
19 Z. Chen, Y. C. Qin, D. Weng, Q. F. Xiao, Y. T. Peng, X. L. Wang, H. X. Li, F. Wei and Y. F. Lu, *Adv. Funct. Mater.*, 2009, **19**, 3420.
20 Z. Chen, V. Augustyn, J. Wen, Y. W. Zhang, M. Q. Shen, B. Dunn and Y. F. Lu, *Adv. Mater.*, 2011, **23**, 791.
21 S. D. Perera, B. Patel, N. Nijem, K. Roodenko, O. Seitz, J. P. Ferraris, Y. J. Chabal and K. J. Balkus, *Adv. Energy Mater.*, 2011, **1**, 936.
22 Y. Yang, L. Li, H. L. Fei, Z. W. Peng, G. D. Ruan and J. M. Tour, *ACS Appl. Mater. Interfaces*, 2014, **6**, 9590.
23 C. Zhou, Y. W. Zhang, Y. Y. Li and J. P. Liu, *Nano Lett.*, 2013, **13**, 2078.
24 T. Qian, C. F. Yu, S. S. Wu and J. Shen, *J. Mater. Chem. A*, 2013, **1**, 6539.
25 T. Qian, X. Zhou, C. F. Yu, S. S. Wu and J. Shen, *J. Mater. Chem. A*, 2013, **1**, 15230.
26 J. Y. Ji, L. L. Zhang, H. X. Ji, Y. Li, X. Zhao, X. Bai, X. B. Fan, F. B. Zhang and R. S. Ruoff, *ACS Nano*, 2013, **7**, 6237.
27 M. J. Deng, C. C. Wang, P. J. Ho, C. M. Lin, J. M. Chen and K. T. Lu, *J. Mater. Chem. A*, 2014, **10**, 1039.
28 J. X. Zhu, L. J. Cao, Y. S. Wu, Y. J. Gong, Z. Liu, H. E. Hoster, Y. H. Zhang, S. T. Zhang, S. B. Yang, Q. Y. Yan, P. M. Ajayan and B. Vajtai, *Nano Lett.*, 2013, **13**, 5408.
29 P. H. Yang, X. Xiao, Y. Z. Li, Y. Ding, P. F. Qiang, X. H. Tan, W. J. Mai, Z. Y. Lin, W. Z. Wu, T. Q. Li, H. Y. Jin, P. G. Liu, J. Zhou, C. P. Wong and Z. L. Wang, *ASC Nano*, 2013, **7**, 2617.
30 B. Saravanakumar, K. K. Purushothaman and G. Muralidharan, *ACS Appl. Mater. Interfaces*, 2012, **4**, 4484.
31 Y. Yang, S. P. Albu, D. Kim and P. Schmuki, *Angew. Chem.*, 2011, **123**, 9237.
32 Y. Yang, D. Kim, M. Yang and P. Schmuki, *Chem. Commun.*, 2011, **47**, 7746.
33 G. Wang, X. Lu, Y. Ling, T. Zhai, H. Wang, Y. Tong and Y. Li, *ACS Nano*, 2012, **6**, 10296.
34 A. Bahloul, B. Nessark, E. Briot, H. Groult, A. Mauger, K. Zaghib and C. M. Julien, *J. Power Sources*, 2013, **240**, 267.
35 K. B. Hatzell, L. Fan, M. Beidaghi, M. Boota, E. Pomerantseva, E. C. Kumbur and Y. Gogotsi, *ACS Appl. Mater. Interfaces*, 2014, **6**, 8886.
36 Z. S. Wu, W. C. Ren, D. W. Wang, F. Li, B. L. Liu and H. M. Cheng, *ACS Nano*, 2010, **10**, 5835.
37 Y. M. He, W. J. Chen, X. D. Li, Z. X. Zhang, J. C. Fu, C. H. Zhao and E. Q. Xie, *ACS Nano*, 2013, **1**, 174.
38 Z. B. Lei, J. T. Zhang and X. S. Zhao, *J. Mater. Chem.*, 2012, **22**, 153.